JOURNAL OF MATERIALS SCIENCE 30 (1995) 980–988

R-curves of an yttria- and alumina-doped hot-pressed silicon nitride ceramic at 1200 °C and room temperature

C. T. BODUR
Department of Materials Science, University of Technology, Sydney, 15-73 Broadway, Sydney, New South Wales 2007, Australia

An energy approach has been utilized to measure the *R*-curves of an Y_2O_3–Al_2O_3-doped hot-pressed silicon nitride ceramic at 1200 °C in an argon atmosphere in three-point bending. In order to evaluate the *R*-curves at 1200 °C, a low constant displacement rate of $\dot{\delta} = 5\ \mu m\ min^{-1}$ was applied in cyclic loading to obtain the cyclic loading/unloading–displacement curves during controlled-crack propagation. Propagated crack lengths were measured directly by a microscope and they were compared to compliance-calculated crack lengths. After digitizing the cyclic load–displacement and crack length–displacement curves, crack-resistance parameters, *R*-curves and *K*-curves, were calculated by computer. At 1200 °C this material behaved non-elastically and the crack parameters, obtained here, represent the non-elastic ones. For comparison, at room temperature, continuous loading was applied to obtain the load–displacement curves. At room temperature, linear–elastic fracture mechanics behaviour was observed.

1. Introduction

Good high-temperature properties of dense Si_3N_4 ceramics [1] (high strength, toughness, creep and thermal shock and relatively good oxidation resistance) make these materials ideal candidates for high-temperature structural applications.

Hot-pressed silicon nitrides (HPSNs) are produced from powders of Si_3N_4 (mainly α-Si_3N_4) and various additives (MgO, Al_2O_3, Y_2O_3, etc.) at high temperatures (≈ 1700 °C) and at high pressures (≈ 30 MPa). The sintering occurs by the liquid-boundary phase which is formed by the additives, various impurities (calcium, iron, aluminium, etc.) and oxide phases, SiO_2 and Si_2N_2O. The microstructure of the hot-pressed silicon nitride contains three phases: prismatic Si_3N_4 grains (90%–95% β-Si_3N_4 and 5%–10% α-Si_3N_4) as the main crystalline phase, secondary crystalline phases and the amorphous grain-boundary phase which results from the liquid phase after the sintering process. At high temperatures, i.e. > 1000 °C, this amorphous grain-boundary phase becomes viscous and controls the various properties, e.g. creep, toughness, strength and oxidation of the hot-pressed silicon nitrides.

It is important to know the strength behaviour of HPSNs at high temperatures where they would be used as structural materials. At low temperatures these materials are brittle and behave linear-elastically, however, at high temperatures, i.e. > 1000 °C, non-elastic properties are observed. Usually, the strength behaviour of ceramics is characterized by fracture toughness measurements (i.e. resistance to crack propagation). To evaluate the fracture toughness of ceramics at low temperatures standard fracture toughness measurements (ASTM E399 [2], linear-elastic fracture mechanics) could be utilized. But at high temperatures these materials behave non-elastically and to evaluate the strength behaviour, i.e. crack resistance parameters, *R*-curves, standard measurement method (ASTM E813 [3], non-elastic fracture mechanics) could be applied. Another, more accurate, method to characterize the *R*-curve behaviour of non-elastic materials, was introduced by Sakai *et al.* [4]. The energy method of Sakai *et al.* was previously discussed theoretically by Eftis and Liebowitz [5]. This method was later used by Gomina [6] to evaluate the *R*-curves of composite materials.

In this work, similar to Sakai *et al.*'s method, an energy approach was used to evaluate the *R*-curves of an HPSN ceramic material at 1200 °C. As a comparison, room-temperature fracture experiments were performed to obtain the linear-elastic fracture curves.

2. The crack energy evaluation method at 1200 °C

In order to observe the load–displacement behaviour at 1200 °C during a controlled-crack growth, a continuous load was applied at a constant displacement rate of $5\ \mu m\ min^{-1}$ to a single-edge notched bending specimen of the HPSN (see Fig. 1). Contrary to the

---

Present address: Graduate School of Biomedical Engineering, The University of New South Wales, Sydney 2052, Australia.

0022–2461

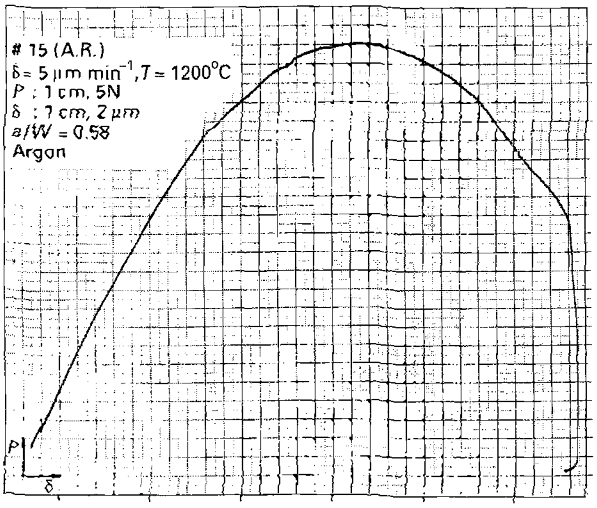

Figure 1 Original plot of the continuous load–displacement curve at 1200 °C; displacement rate, $\dot{\delta} = 5\ \mu\text{m min}^{-1}$.

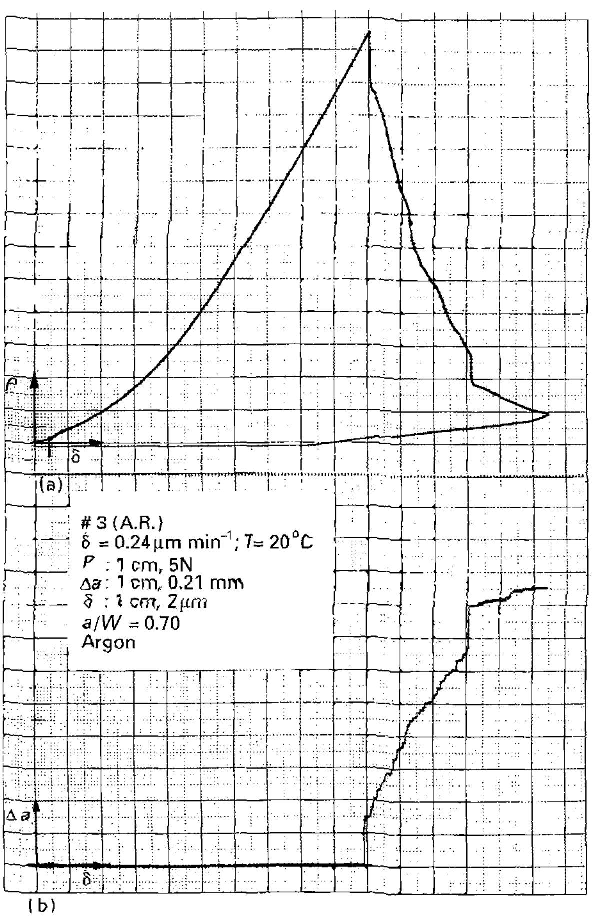

Figure 2 Original plot at room temperature; displacement rate, $\dot{\delta} = 0.24\ \mu\text{m min}^{-1}$: (a) continuous load–displacement curve; (b) optical measured crack length–displacement curve.

sharp maximum load, during a similar measurement at room temperature (see Fig. 2), which would be observed when the crack starts to propagate (i.e. linear-elastic behaviour [7]), at 1200 °C the load–displacement curve shows a plateau maximum with large displacement (i.e. non-elastic behaviour). It would not be possible to evaluate the correct crack propagation energy using this curve (Fig. 1, i.e. it would be necessary for the crack energy to be separated from the total energy, consumed during loading). For this reason, instead of continuous loading, loading/unloading cycles were performed to calculate the crack-propagation energies. In Fig. 3a, an original loading/unloading-displacement curve of a controlled-crack growth measurement at 1200 °C is presented. Similarly, in order to evaluate the crack-propagation energies, crack growth, Δa, was measured at the same displacement rate (Fig. 3b). In Fig. 3b, the actual crack lengths at each displacement are marked by points (i.e. the crack lengths were measured after each unloading cycle). It is observed from Fig. 3a that the loading/unloading curves did not meet at the origin, but they resulted in permanent displacements, i.e. plastic effects.

During loading, the work, ΔW, applied to a specimen to create a Δa crack length was consumed by the elastic deformation energy, U_{el}, irreversible energy, U_{ir}, and the crack energy, Γ

$$\frac{\partial W}{\partial A} = \frac{\partial U_{\text{el}}}{\partial A} + \frac{\partial U_{\text{ir}}}{\partial A} + \frac{\partial \Gamma}{\partial A} \tag{1}$$

where $\partial W/\partial A$ is the total work per unit crack surface, $\partial U_{\text{el}}/\partial A$ the elastic energy per unit crack surface, $\partial U_{\text{ir}}/\partial A$ the irreversible energy per unit crack surface, and $\partial \Gamma/\partial A$ the crack propagation energy per unit crack surface, with A (the crack surface) = Ba, where B is the specimen thickness, and a the crack length.

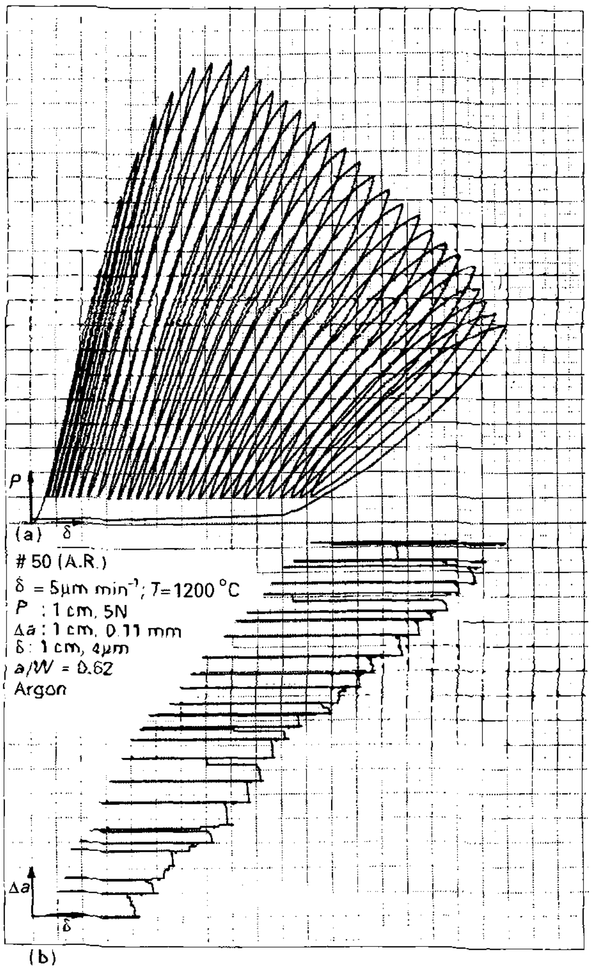

Figure 3 Original plot at 1200 °C; displacement rate, $\dot{\delta} = 5\ \mu\text{m min}^{-1}$: (a) cyclic loading/unloading–displacement curve; (b) optical measured crack length–displacement curve (actual crack lengths are marked by points).

The irreversible energy, U_{ir}, in general, could be caused by the following mechanisms:

(i) development of microcracks in a process zone in the crack-front [8];

(ii) friction due to the grains and fibres [9–11] and development of bridges from the viscous second phase [9, 12, 13] between the crack surfaces behind the crack front.

Using Equation 1, a non-linear-elastic crack propagation energy rate (i.e. energy spent to create a unit crack surface) can be defined as

$$\tilde{G}_c = \frac{\partial[W - (U_{el} + U_{ir})]_c}{\partial A} = \frac{\partial \Gamma}{\partial A} \tag{2}$$

In the linear-elastic case (i.e. $\Delta U_{ir} \to 0$) and $\tilde{G}_c \to G_c$.

The crack resistance parameter, R (i.e. the total energy spent to create a unit crack surface), can be defined as

$$R = \frac{\partial(W - U_{el})_c}{\partial A}$$

$$= \frac{\partial U_{ir}}{\partial A} + \frac{\partial \Gamma}{\partial A} \tag{3}$$

or

$$R = \tilde{G}_c + \phi_{ir} \tag{4}$$

with

$$\phi_{ir} = \frac{\partial U_{ir}}{\partial A} \tag{5}$$

When $\phi_{ir} \to 0$, $R \to \tilde{G}_c \to G_c$. Schematic diagrams of these energies are presented in Fig. 4a and b by approximating Fig. 3a.

The aim of the fracture mechanical investigation of this work was to obtain the necessary data to characterize the HPSN material at 1200 °C. When G_c could be evaluated by the energy method of this work, K_{Ic} would be readily calculated from $G_cE' = K_{Ic}^2$ [7], which is valid for the plane-strain condition, with $E' = E/(1 - \nu)$, where E is Young's modulus and ν is Poisson's ratio.

In this work, in order to evaluate the elastic crack-propagation energy, $\tilde{G}_c$, the load–displacement by the loading/unloading cycles (e.g. Fig. 3a) and the crack length–displacement (e.g. Fig. 3b) measurements had to be utilized to obtain the elastic load–displacement and crack length–displacement curves. Then by using Equation 2, which in this case $U_{ir} = 0$, $\tilde{G}_c$ could be calculated. Separation of the elastic crack energy, $\Delta U_{\tilde{G}}$ from the total energy (ΔU_R) (see Fig. 4a, b) is schematically shown in Fig. 5a and b. Each original loading/unloading cycle, as in Fig. 3a, obtained from the controlled-crack growth measurements is displaced in parallel to the origin. An approximation was made here about the loading/unloading curves which show hysteresis (see Fig. 3a). These hystereses could be due to the different effects, friction between the loading rods and the specimen [14], friction between the crack surfaces during unloading/loadings, and the viscous effects of the amorphous phase [4]. In order to make the calculations less complicated, each loading/unloading curve was approximated to a straight line to obtain the modified loading/unloading curves. Each i line (Fig. 5a) was created by using the maximum load point of the $(i - 1)$th curve and a tangent drawn from that point to the ith loading curve – during the reloading of the specimen (ith curve), it was observed from the video picture of the crack that the crack started to re-open at that particular tangent point. After displacing each modified loading/unloading curve (i.e. lines) parallel to the origin, a non-linear load–displacement curve (the dashed curve in Fig. 5b) was obtained. In a similar way the crack length–displacement curve was displaced by maintaining its crack length at a given load value (the dashed curve in Fig. 5b). After the modified load–displacement and modified crack length–displacement curves were obtained, non-linear elastic crack energy, $\tilde{G}_c$ values (i.e. $\tilde{G}_{c,R}$ curve), could be calculated by the elastic fracture mechanics (see, for example, [13]). K_c values (i.e. K_R curve) could also be calculated from the $\tilde{G}_c$($\tilde{G}_{c,R}$ curve) by using the plane-strain condition relation, i.e. $G_cE' = K_{Ic}^2$. The extrapolation of these curves ($\tilde{G}_{c,R}$ and K_R) to $\Delta a \to 0$ (i.e. to the notch length) would result in the conservative $\tilde{G}_c$ and K_{Ic} values, respectively.

In this work, in addition to the direct measured crack lengths, analytical crack lengths were calculated by using the elastic load–displacement curves by the formula [9],

$$a_i = a_{i-1} + \left(\frac{W - a_{i-1}}{2}\right)\left(\frac{C_i - C_{i-1}}{C_i}\right) \tag{6}$$

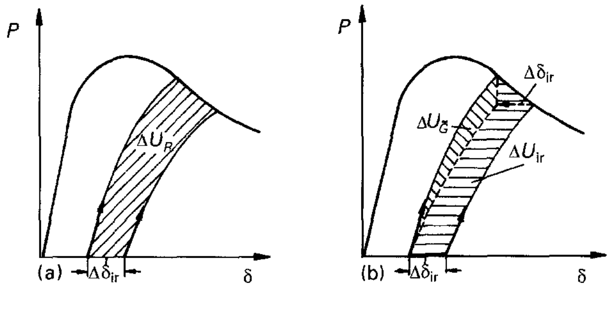

Figure 4 Non-elastic load–displacement curve: (a) total energy, ΔU_R, consumed during the Δa crack propagation; (b) non-linear-elastic crack energy, $\Delta U_{\tilde{G}}$, and irreversible crack energy, ΔU_{ir}, during the Δa crack propagation.

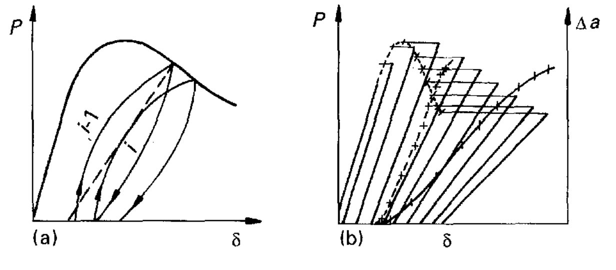

Figure 5 Separation of the non-linear-elastic curve from the non-elastic curve: (a) linearization of the loading/unloading cycles; (b) obtaining the non-linear-elastic load–displacement and crack length–displacement curves by the separation method (i.e. shifting the irreversible displacements to the origin).

where a_i is the ith crack length, C_i the ith compliance value, and W the specimen height.

3. The crack energy evaluation at room temperature

At room temperature this material behaved in a linear elastic manner (see Fig. 2), and for this reason it was not necessary to use the loading/unloading, but instead continuous loading could be applied to a notched specimen at a constant displacement rate in order to observe the controlled-crack growth. In Fig. 2a a continuous load–displacement curve of a notched bending specimen is shown, with the crack propagation curve in Fig. 2b. These curves show linear-elastic fracture mechanics behaviour, i.e. crack starts at the sharp maximum load point and there are no plastic effects (when the specimen was unloaded to zero load, there was no permanent displacement). From these curves, Fig. 2a and b, crack-energy parameters (G and K) could be readily calculated for the linear-elastic case [7].

4. Experimental procedure

4.1. Material

The material of this investigation was a 8% Y_2O_3 and 2% Al_2O_3 (by weight) doped hot-pressed silicon nitride ceramic. Specimens were supplied by ESK Kempten, Germany. The manufacturer's data of the starting powders before the fabrication of the HPSN are given in Table I. The density of the material was measured by the suspension method in CCl_4, $\rho = 3.28\,g\,cm^{-3}$. Three-point bending strength at room temperature was 923 ± 51 MPa. The dimensions of the specimens were $3.5 \times 7 \times 35\,mm^3$.

4.2. Experimental conditions

In order to observe and measure the crack lengths under a travelling microscope, the specimens were polished to 3 μm with diamond paste. The specimens were single-edge notched to relative crack lengths of $a/W \approx 0.6$ for the 1200 °C measurements and $a/W \geqslant 0.65$ for the room-temperature measurements with diamond blades of thickness of about 70 μm. The loading was applied at a constant displacement rate to achieve the controlled-crack growth in three-point bending with span length of 30 mm. In order to avoid subcritical-crack growth, measurements were performed in an inert atmosphere, argon of purity 99.999%. The loading to the specimens were applied by SiC rods. The measurements were done with a servo-hydraulic tension/ compression testing machine (Type PSA 04, Schenk). The high temperatures up to 1500 °C were achieved by induction heating with a middle frequency generator. Crack lengths were measured manually by observing the video picture of the crack propagation through a travelling microscope which followed the crack front. Load–displacement, P-δ, and crack length–displacement, $\Delta a - \delta$, curves were plotted during the controlled-crack growth measurements. After they were digitized, the crack parameters R, G and K values were calculated by computer.

TABLE I Manufacturer's data of the starting powders

Chemical analysis of Si_3N_4 powder (wt%)

N_2	O_2	C	Ca	Al	Fe	Mg	Si
37.9	1.9	0.3	0.25	0.22	0.2	0.08	the rest

Grain size: 97% < 10.6 μm, 50% < 1.6 μm, 6% < 0.6 μm

Specific surface area: $6.1\,m^2\,g^{-1}$

Modification: 96% α-Si_3N_4, 4% β-Si_3N_4

Additives: 8 wt% Y_2O_3, 2 wt% Al_2O_3

In order to calculate the K values from the G values, elastic constants, Young's modulus, E, and Poisson's ratio, ν were needed. Elastic constants, Young's modulus, E, and shear modulus, G, were measured from room temperature to 1250 °C in air using a resonance method [15]. Poisson's ratios were calculated from the elasticity theory, $\nu = (E/2G) - 1$ [16].

In order to achieve controlled-crack growth, low constant displacement rates were applied during loading. Preliminary experiments were performed at 1200 °C, by varying the constant displacement rates of 1, 5, 7.5 and $10\,\mu m\,min^{-1}$ for loadings during crack growth and with various constant loading/unloading cycles displacement rates of 5, 50, 75 and $100\,\mu m\,min^{-1}$ to obtain the optimal experimental conditions for the controlled-crack propagation. When the constant displacement rate was low the measurements lasted a long time, e.g. at $\dot{\delta} = 1\,\mu m\,min^{-1}$ for about $\Delta a = 3$ mm crack propagation, the loading/unloading cycle measurement was about 9 h. This caused high plasticity in the load–displacement curve. At this rate, creep was the dominant crack-growth mechanism instead of the loading stresses (i.e. the aim here was to obtain the R-curves in such a way as to understand the mechanism of crack propagation from the fracture mechanics point of view). At $\dot{\delta} = 10\,\mu m\,min^{-1}$, loading was so fast that the controlled-crack growth was not succeeded, i.e. fracture occurred in a sudden behaviour. After these trials, the optimal displacement rate for the loading was chosen as $\dot{\delta} = 5\,\mu m\,min^{-1}$ and this rate was also applied for the loading/unloading cycles. At this rate, the controlled-crack growth was achieved and the measurements did not last so long (about 4 h), so that the creep crack effects could be minimized. Loading/unloading cycles could be done either at the same displacement rate as the loading or at a higher displacement rate. The aim was again to perform the measurements at 1200 °C in as short a time as possible in order to minimize the creep effects. For this reason, the displacement rates for the loading/unloading cycles were first tried at much higher rates than the loading displacement rates, e.g. $\dot{\delta} = 1\,\mu m\,min^{-1}$ for the loading and $\dot{\delta} = 100\,\mu m\,min^{-1}$ for the loading/unloading cycles, or $\dot{\delta} = 7.5\,\mu m\,min^{-1}$ and $\dot{\delta} = 75\,\mu m\,min^{-1}$, respectively, etc. But this also created some problems. First of all, the loading/unloading cycle displacement rate was so high (e.g. $\dot{\delta} = 100\ \mu m\ min^{-1}$) that at the maximum load level, it was quite difficult to change the displacement rate back to its loading value (e.g. back to $\dot{\delta} = 1\ \mu m\ min^{-1}$) while correctly measuring the crack length and without causing fracture (i.e. fast fracture). The other effect was that the slopes of the loading/unloading curves were controlled by the value of the displacement rates. The higher the displacement rates were, the higher were the slopes. This also complicated the measurements and the evaluation method of the R-curves. For these reasons the same displacement rate of $\dot{\delta} = 5\ \mu m\ min^{-1}$ was applied both to the loading and the loading/unloading cycles at 1200 °C. At room temperature, $\dot{\delta} = 0.24\ \mu m\ min^{-1}$ was needed to be applied in continuous loading to achieve the controlled-crack growth (see Fig. 2). At 1200 °C in loading/unloading measurements, loading was permitted until a measurable crack length was observed on the video screen, then before any further load increase, the specimens were unloaded. Unloading was applied not to the zero load level, but to a level of about 5 N to remain in contact with the specimens, otherwise instabilities occurred and the specimens failed by fracture. After this load level of unloading, the specimens were re-loaded.

5. Results and discussion

The results of Young's modulus, E, shear modulus, G, and Poisson's ratio, ν, from the resonant measurements in the range of room temperature to 1250 °C are given in Fig. 6. It was calculated that at room temperature, $E = 309$ GPa, $G = 117$ GPa, $\nu = 0.32$, and at 1200 °C, $E = 274$ GPa, $G = 104$ GPa, $\nu = 0.32$. The values of elastic constants, E and G, decreased from room temperature to about 800 °C linearly, and above 900 °C they decreased in much higher rate. This behaviour of the elastic constants at temperatures $\geqslant 900$ °C is due to the amorphous (i.e. viscous) grain-boundary phase [17, 18].

By evaluating the digitized experimental values of P–δ and Δa–δ (see Fig. 3a and 3b) on a computer, various results are presented in Fig. 7a–e. Fig. 7a shows the digitized load–displacement, P–δ, curve and the optical measured crack length–displacement, Δa–δ, curve. The R-curve calculated using Equation 3 by measuring the ΔU_R areas (see Fig. 4) from the original P–δ and Δa–δ curves (Fig. 3a, b) is shown in Fig. 7b. Fig. 7c shows the non-linear elastic load–displacement curve obtained using the separation of energies method (method in Fig. 5b, i.e. $\Delta\delta_{ir} \rightarrow 0$), the optical measured crack length after the separation method (Fig. 5b) and the crack length calculated from Equation 6 using the compliance of the non-linear elastic load–displacement curve, P–δ curve in Fig. 7c. It is seen in Fig. 7c, that the crack length calculated from Equation 6 matches the optically measured crack length. This confirms the accuracy of the separation method. The non-linear elastic crack energy rate, $\tilde{G}$, calculated from the curves of Fig. 7c, i.e. P–δ and Δa–δ, by the method of separation of energies (see Fig. 5b, is shown in Fig. 7d. K_{Ic} values calculated from the $\tilde{G}$ values (Fig. 7d) using the plane-strain relation, $GcE' = K_{Ic}^2$ are given in Fig. 7e. The increasing K_R curve in Fig. 7e with the relative crack length, a/W, does not represent the linear elastic fracture mechanics case (i.e. in the linear elastic fracture mechanics, the G_R and K_R curves would be constant with the crack length). When $\Delta a \rightarrow 0$, i.e. when the crack length is just equal to the notch length, $\phi_{ir} \rightarrow 0$ and the K_R curve could be extrapolated to the K-axis to obtain the fracture toughness, K_{Ic}, of the material.

In comparison with the 1200 °C measurements continuous-loading RT measurements resulted in the various curves shown in Fig. 8a–c. They were obtained by evaluating the measured load–displacement and crack length–displacement curves (see P–δ and Δa–δ in Fig. 2a, b). Fig. 8a shows the digitized

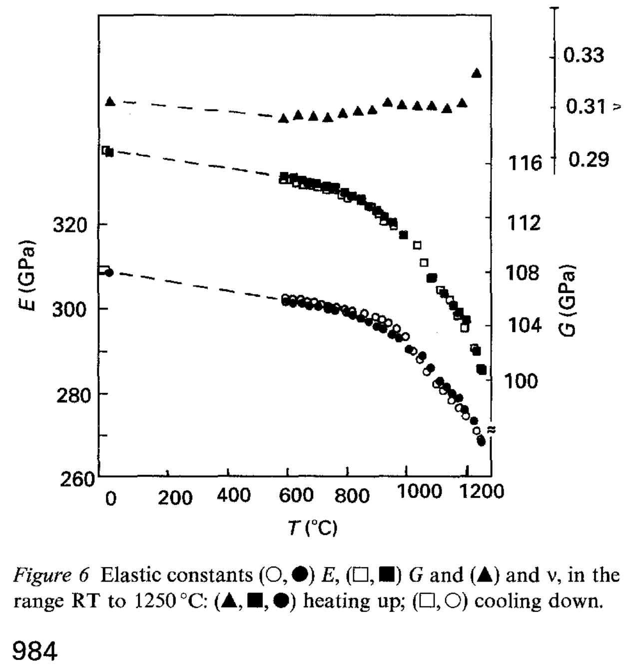

Figure 6 Elastic constants (○, ●) E, (□, ■) G and (▲) and ν, in the range RT to 1250 °C: (▲, ■, ●) heating up; (□, ○) cooling down.

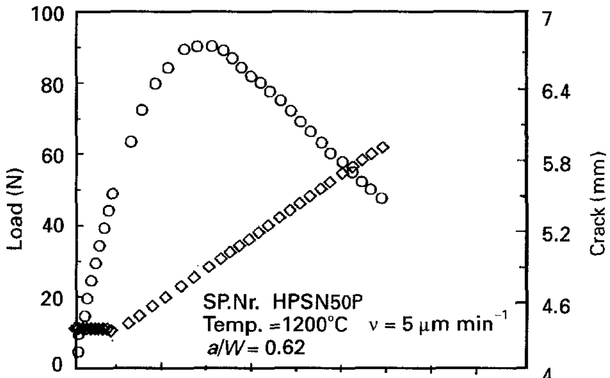

Figure 7(a) (○) Load–displacement curve and (◇) the optical measured crack length–displacement curve; 1200 °C. (b) Total crack-resistance energy with relative crack length; 1200 °C. (c) (○) Load–displacement curve and the crack length–displacement curves (◇), optically measured and (▷) compliance-calculated crack lengths, after the separation method; 1200 °C. (d) Non-linear-elastic crack energy with the relative crack lengths, calculated using (◇) the optically measured and (▷) the compliance-calculated crack lengths; 1200 °C. (e) K-values (K_R-curve) calculated from the non-linear-elastic crack energy values with the relative crack lengths, (◇) optically measured and (▷) compliance-calculated crack lengths; 1200 °C.

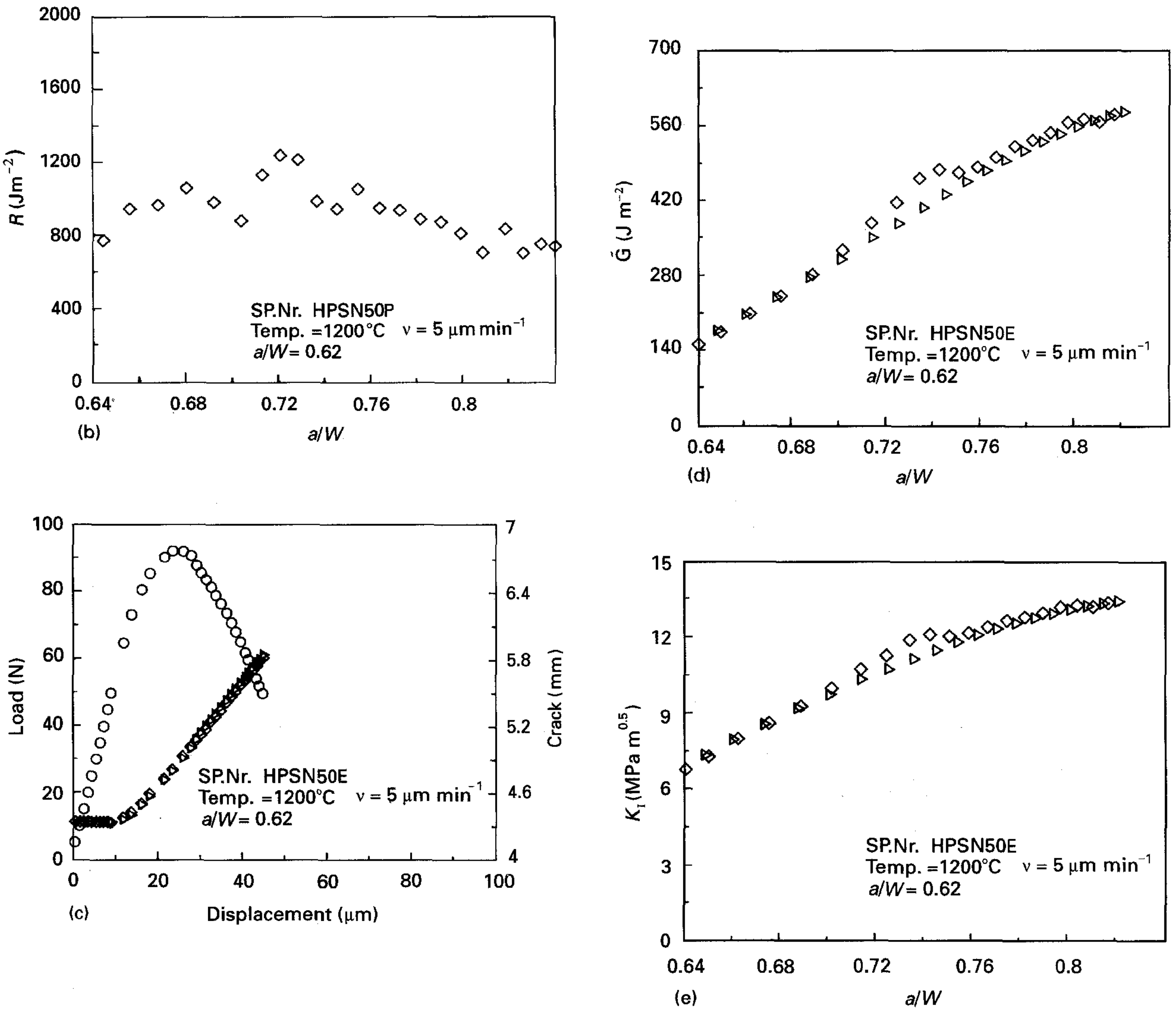

Figure 7 (*continued*)

load–displacement curve together with the measured and compliance-calculated crack lengths, while the linear-elastic crack energy rate, G, calculated from the load–displacement and crack length–displacement curves of Fig. 8a, are given in Fig. 8b. K_{Ic} values calculated from the G values (from Fig. 8b) both for the optically measured and the compliance-calculated crack lengths, are shown in Fig. 8c. K values of this K_R curve represent the linear-elastic values, i.e. $K = K_{Ic} \cong \text{constant} \cong 7\ \text{MPa}\,\text{m}^{1/2}$.

At 1200 °C, R-curves obtained from Equation 3 remained relatively constant, about $1000\ \text{J}\,\text{m}^{-2}$, with the relative crack lengths (Fig. 7b). The crack-propagation energy, $\tilde{G}_c$ (Fig. 7d), obtained from the separation method is much lower than the R value. The difference in these values is the irreversible crack energy rate, ϕ_{ir} (Equation 5), which is the consumed energy in front of the crack front (i.e. microcracking), behind the crack front (i.e. friction effects, bridging effects, secondary phase effects), and the energy consumed by crack branching.

The $\tilde{G}_R$ (K_R) curves in Fig. 7d and e show the increasing behaviour with the relative crack lengths, a/W. This could be attributed to the viscous behaviour of the amorphous phase (i.e. this phase weakens above 1000 °C). Contrary to this, the increasing R-curve behaviour of metallic materials is due to the

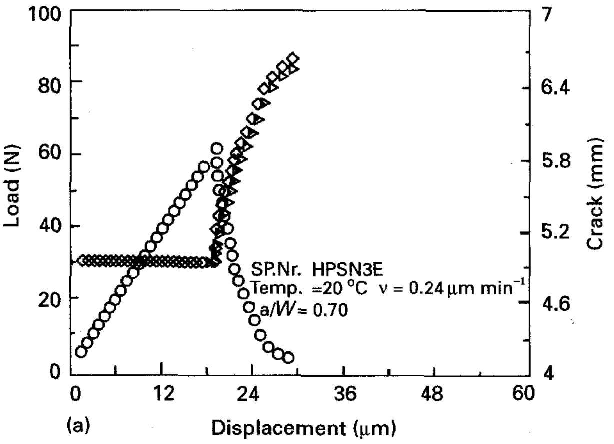

Figure 8(a) (○) Load–displacement curve and the crack length–displacement curve, (◇) optically measured and (▷) compliance-calculated crack lengths; room temperature. (b) Linear-elastic crack energy with the relative crack lengths, calculated using (◇) the optically measured and (▷) compliance-calculated crack lengths; room temperature. (c) K-values (K_R-curve) calculated from the linear-elastic crack energy values with the relative crack lengths, (◇) optically measured and (▷) compliance-calculated crack lengths; room temperature.

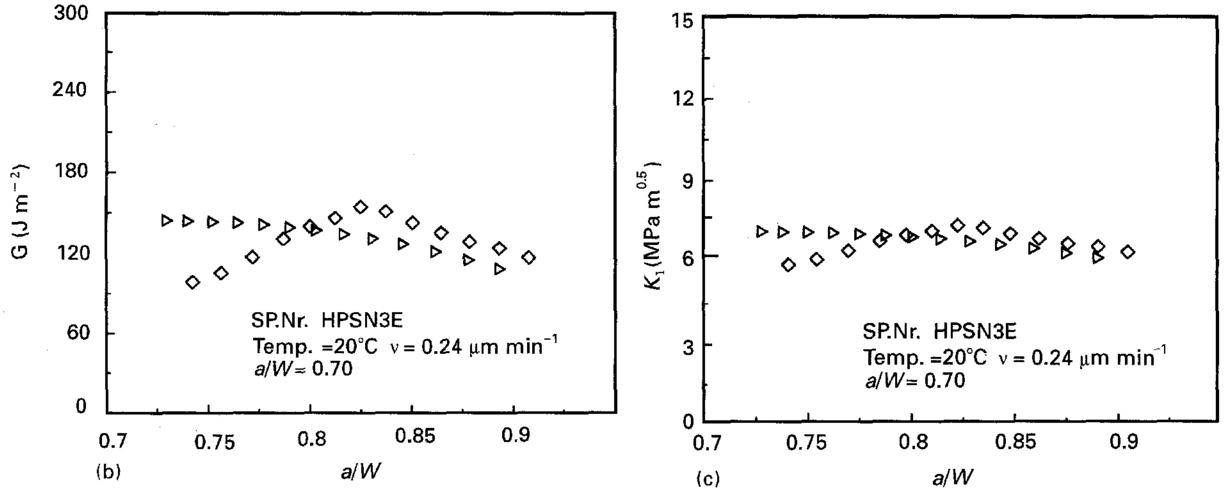

Figure 8 (*continued*)

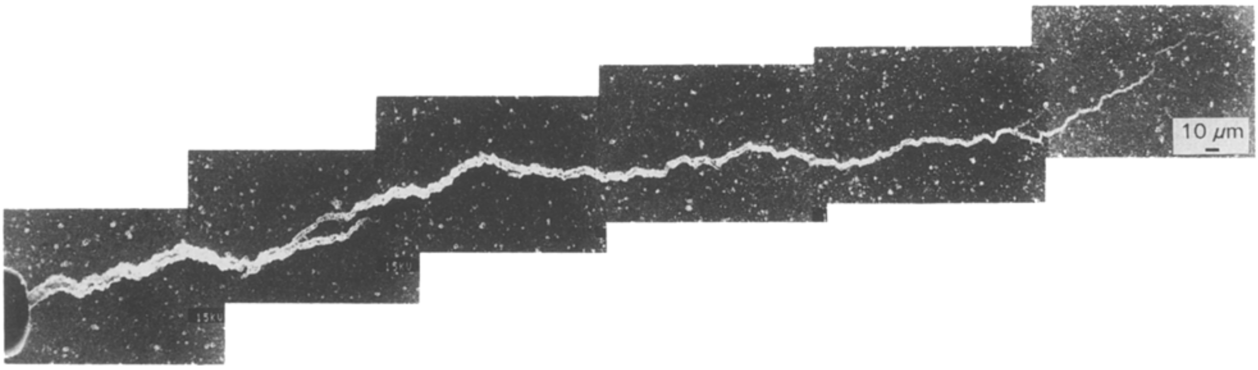

Figure 9 Scanning electron micrographs showing a typical controlled-crack propagation at 1200 °C.

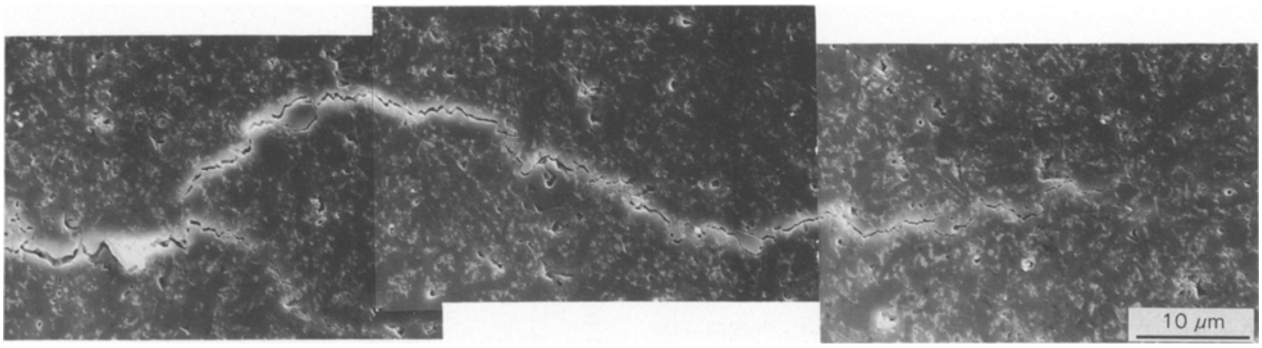

Figure 10 Scanning electron micrographs showing the crack propagation in controlled-crack growth at 1200 °C.

plastic zone at the crack front [13]. In comparison with the 1200 °C $\tilde{G}_R$ (K_R) curves, the room-temperature fracture energy curves (G_R, K_R, see Fig. 8b and c) are almost constant with the relative crack length a/W – at room temperature this material behaved linear-elastically.

Fig. 9 shows scanning electron micrographs of a typical controlled-crack propagation at 1200 °C. A detailed area of the controlled-crack-growth is presented in Fig. 10. Crack-resistance effects could be explained with these micrographs. Contrary to the ideal linear-elastic fracture mechanical crack propagation, this crack does not follow a straight line; crack branches and microcracks exist which all consume energy because they do not just produce a single, straight, crack surface of which the energy consumption ideally would be G_c. All these effects (crack branching, microcracks, friction effects (mainly caused by the larger grains), secondary (i.e. amorphous) phase effects (viscoelastic behaviour)) contribute to the irreversible crack energy, ϕ_{ir}. Figs. 11 and 12 show scanning electron micrographs of the details from Fig. 10, with the crack branching and micro cracks. Fig. 13 shows details from Fig. 12, of the second-phase

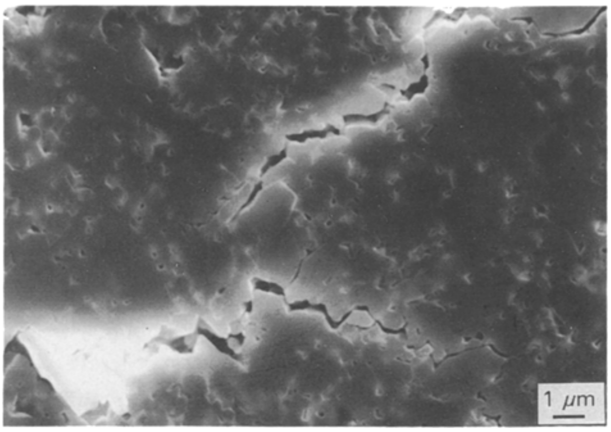

Figure 11 Scanning electron micrograph showing the details from Fig. 10.

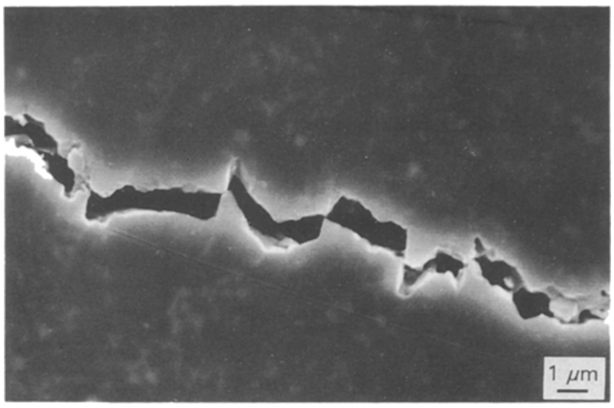

Figure 14 Scanning electron micrograph showing the crack behaviour during the controlled-crack growth at room temperature.

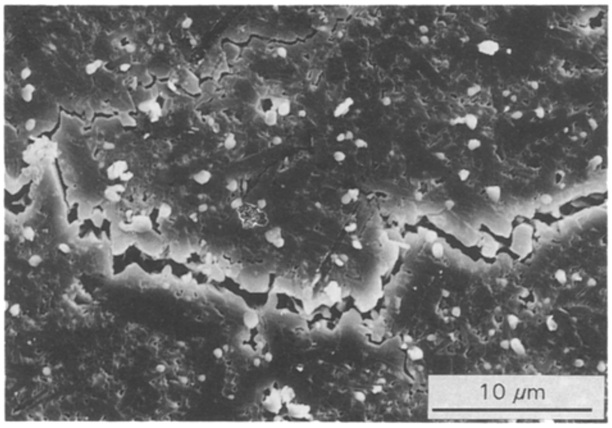

Figure 12 Scanning electron micrograph showing the crack path following the grain boundaries (friction effects).

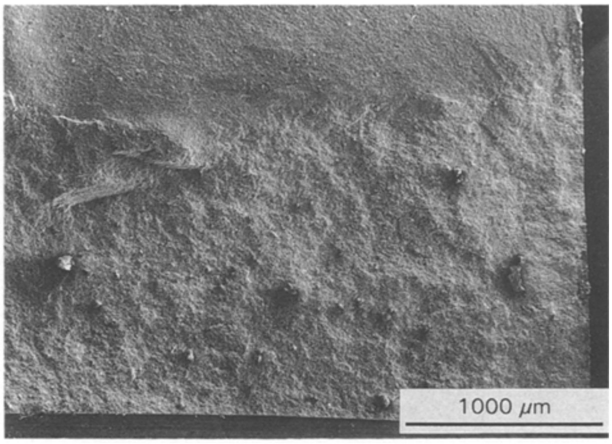

Figure 15 Scanning electron micrograph showing the fracture surface of a specimen at 1200 °C. Notch surface (bottom), controlled-crack growth (i.e. slow crack growth) (middle) and the fast fracture (top).

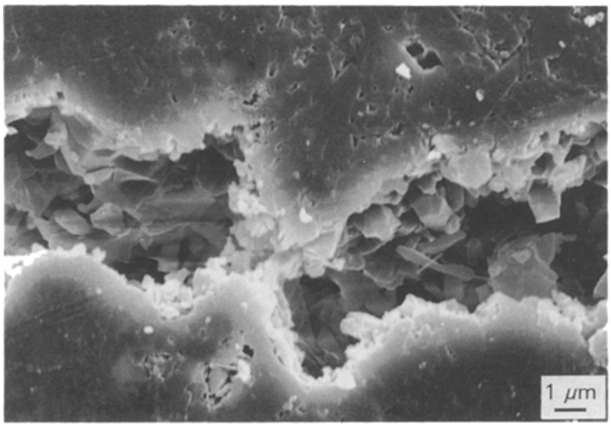

Figure 13 Scanning electron micrograph showing the details from Fig. 12 (grain bridging and the amorphous-phase effects).

effects and crack bridging. It is clearly seen from these pictures that the crack surfaces are not straight, as would be expected from an ideal crack. At high temperatures, here 1200 °C, and low loading rates, here a displacement rate of $\dot{\delta} = 5\ \mu\text{m min}^{-1}$, the crack follows the grain boundaries (i.e. the crack propagates through the relatively weak amorphous phase) which causes the crack surface to take the grain shapes, i.e. mainly large grains, zig-zag shape (Figs 10–13). Contrary to this, the room-temperature measurements show that these effects, i.e. irreversible effects, are minimum at room temperature – the crack propagates almost linear-elastically (see Fig. 14). This means that at room temperature during loading, all the energy consumed, other than elastic energy, is invested only for crack propagation, i.e. $\phi = 0$ and $R = G$.

In Fig. 15, it is observed from the crack surface (lower part in Fig. 15) of a specimen that the crack propagation during the controlled-crack growth was intergranular at 1200 °C. The crack follows the amorphous phase – the crack surface is rough. The upper part of Fig. 15 shows the fast fracture region which represents the transgranular fracture (i.e. smooth surface). Figs 16 and 17 show details from Fig. 15. Fig. 16 represents the surface area of the slow-crack growth region where the fracture was intergranular, i.e. long prismatic β-Si_3N_4 grains are unbroken. Fig. 17 shows the fast fracture region, which is smoother than the slow-crack growth region, i.e. fracture is transgranular – long prismatic β-Si_3N_4 grains are broken. At room temperature the fracture

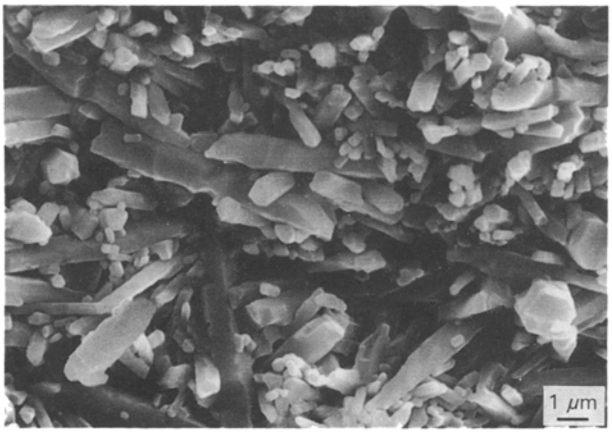

Figure 16 Scanning electron micrograph showing the details from Fig. 15, of the controlled-crack growth (i.e. slow crack growth) region. The crack surface is intergranular.

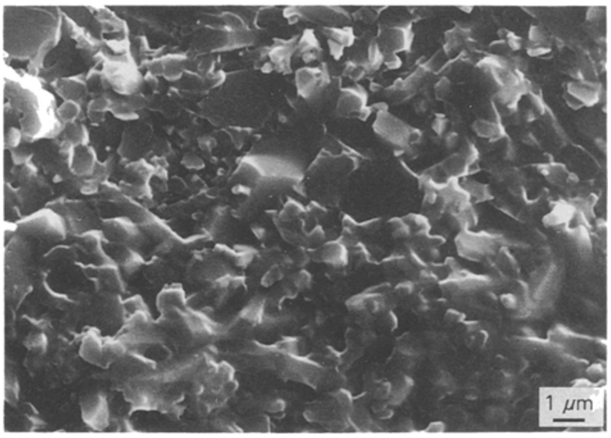

Figure 17 Scanning electron micrograph showing the details from Fig. 15, fast fracture region. The fracture surface is transgranular.

Figure 18 Scanning electron micrograph showing the fracture surface of the controlled-crack growth region of a specimen at room temperature. The fracture surface is mainly transgranular.

surface was mainly transgranular (Fig. 18). This would be expected, because the effects of amorphous phase are negligible at low temperatures, i.e. the material fractured linear-elastically.

6. Conclusion

Three-point bend tests were applied to an Y_2O_3–Al_2O_3- doped hot-pressed silicon nitride ceramic in an argon atmosphere at 1200 °C and at room temperature to obtain the *R*-curves.

At room temperature, linear-elastic fracture mechanics behaviour was observed. At 1200 °C the material behaved non-elastically, where large irreversible displacements were observed during the loading/unloading cycles. Owing to this irreversibility, crack resistance energy, *R*, was not equal to the elastic crack energy, $\tilde{G}_c$, but, $R = \tilde{G}_c + \phi_{ir}$. Here, the irreversible crack energy, ϕ_{ir}, represents the energy consumption in front and behind the crack front.

Acknowledgements

This research work was undertaken at Max-Planck-Institut, Stuttgart, Germany. I thank Professor K. Kromp, University of Vienna, for helpful discussions. Financial support of the "Deutsche Forschungsgemeinschaft" is gratefully acknowledged.

References

1. G. ZIEGLER, J. HEINRICH and G. WOTTING, *J. Mater. Sci.* **22** (1987) 3041.
2. ASTM Standards E399-83 (American Society for Testing and Materials, Philadelphia, PA, 1985) p. 910.
3. ASTM Standards E813-81 (American Society for Testing and Materials, Philadelphia, PA, 1981) p. 768.
4. M. SAKAI, K. URASHIMA and M. INAGAKI, *J. Am. Ceram. Soc.* **66** (1983) 868.
5. J. EFTIS and LIEBOWITZ, *Eng. Fract. Mech.* **7** (1975) 101.
6. M. GOMINA, Habilitation thesis, University of Caen, November, 1987.
7. D. BROEK, "Elementary Engineering Fracture Mechanics" (Sijthoff and Noordhoff, The Netherlands, 1978) p. 115.
8. F. E. BURESCH, *Sci. Ceram.* **7** (1973) 383.
9. A. BORNHAUSER, K. KROMP and R. F. PABST, *J. Mater. Sci.* **20** (1985) 2586.
10. M. SAKAI, J. I. YOSHIMURA, Y. GOTO and M. INAGAKI, *J. Am. Ceram. Soc.* **71** (1988) 609.
11. D. B. MARSHALL, B. N. COX and A. G. EVANS, *Acta Metall.* **33** (1985) 2013.
12. K. KROMP, T. HAUG, R. F. PABST and V. GEROLD, in "Proceedings of the 3rd International Conference on Creep and Fracture of Engineering Materials and Structures, Swansea, edited by B. Wilshire and R. H. Evans, (The Institute of Metals, London, 1987) p. 1021.
13. K. KROMP, in "Brittle Matrix Composites 1", edited by A. M. Brandt and I. H. Marshall (Elsevier, London, 1986) p. 131.
14. R. MOHRMANN, *Fortschr. Deut. Keram. Gesell.* (*Ceram. Forum Int.*) **3** (1988) 137.
15. A. WANNER and K. KROMP, *ibid.* **3** (1988) 43.
16. A. C. UGURAL and S. K. FENSTER, in "Advanced Strength and Applied Elasticity" (American Elsevier, New York, London, Amsterdam, 1975) p. 48.
17. C. T. BODUR, D. V. SZABO and K. KROMP, *J. Mater. Sci.* **28** (1993) 2089.
18. C. T. BODUR, *ibid.*, submitted.

Received 13 October 1993
and accepted 27 July 1994